Обзор ArXiv: astro-ph, 29 мая – 2 июня 2017

От Сильченко О.К.

Astro-ph: 1706.00106

A Unified Model for Galactic Discs: Star Formation, Turbulence Driving, and Mass Transport

Mark R. Krumholz[1⋆], Blakesley Burkhart[2], John C. Forbes[2], and Roland M. Crocker[1]

[1] *Research School of Astronomy & Astrophysics, Australian National University, Canberra, ACT 2611, Australia*
[2] *Harvard-Smithsonian Center for Astrophysics, 60 Garden St, Cambridge, MA 0213, USA*

2 June 2017

ABSTRACT

We introduce a new model for the structure and evolution of the gas in galactic discs. In the model the gas is in vertical pressure and energy balance. Star formation feedback injects energy and momentum, and non-axisymmetric torques prevent the gas from becoming more than marginally gravitationally unstable. From these assumptions we derive the relationship between galaxies' bulk properties (gas surface density, stellar content, and rotation curve) and their star formation rates, gas velocity dispersions, and rates of radial inflow. We show that the turbulence in discs can be powered primarily by star formation feedback, radial transport, or a combination of the two. In contrast to models that omit either radial transport or star formation

Параметры модели – входные и выходные

Symbol	Fiducial Value	Meaning	Defining equation
		Inputs to model	
$\Sigma_{\rm g}$	-	Gas surface density	-
Σ_*	-	Stellar surface density	-
$\sigma_{\rm g}$	-	Gas velocity dispersion (total thermal plus non-thermal)	-
σ_*	-	Stellar velocity dispersion	-
$\rho_{\rm d}$	-	Dark matter density	-
v_ϕ	-	Galaxy rotation curve velocity	-
Ω	-	Galaxy angular velocity	-
$t_{\rm orb}$	-	Galaxy orbital period, $t_{\rm orb} = 2\pi/\Omega$	-
β	0	Rotation curve index, $\beta = d\ln v_\phi d\ln r$	-
$f_{g,Q}$	0.5	Fractional contribution of gas to Q	9
$f_{g,P}$	0.5	Fractional contribution of gas self-gravity to midplane pressure	20
$f_{\rm sf}$	-	Fraction of ISM in star-forming molecular phase	30
		Physics parameters	
$Q_{\rm min}$	1	Minimum possible disc stability parameter	6
$\phi_{\rm mp}$	1.4	Ratio of total pressure to turbulent pressure at midplane	12
η	1.5	Scaling factor for turbulent dissipation rate	26
$\phi_{\rm Q}$	2	One plus ratio of gas to stellar Q	27
$\phi_{\rm nt}$	1	Fraction of velocity dispersion that is non-thermal	28
$\epsilon_{\rm ff}$	0.015	Star formation efficiency per free-fall time	30
$t_{\rm sf,max}$	2 Gyr	Maximum star formation timescale	32
ϕ_a	2	Offset between resolved and unresolved star formation law normalisations	58
		Model outputs	
$\rho_{\rm min}$	-	Minimum midplane density required to produce rotation curve	51
$t_{\rm orb,T}$	-	Orbital period at which galaxies switch from GMC to Toomre regime	33
$\sigma_{\rm sf}$	-	Gas velocity dispersion that can be sustained by star formation alone	39
$\Sigma_{\rm sf}$	-	Gas surface density below which star formation alone can sustain turbulence	41
$\dot{M}_{\rm ss}$	-	Steady-state mass inflow rate	49

Пункт 1: устойчивость по Тоомре

$$Q \approx \left(Q_{\rm g}^{-1} + \frac{2\sigma_{\rm g}\sigma_*}{\sigma_{\rm g}^2 + \sigma_*^2} Q_*^{-1} \right)^{-1} \tag{6}$$

where

$$Q_{\rm g} = \frac{\kappa \sigma_{\rm g}}{\pi G \Sigma_{\rm g}} \tag{7}$$

and similarly for Q_*. Here $\kappa = \sqrt{2(\beta+1)}\Omega$ is the epicyclic frequency. This expression is valid as long as $Q_{\rm g} < Q_*$, the quasi-spherical dark matter halo contributes negligibly to the gravitational stability or instability of the system (i.e., $Q_{\rm d} \gg Q_*$, where $Q_{\rm d}$ is the dark matter Q), and the ratio of vertical to radial velocity dispersions for the gas and stars is $\gtrsim 0.5$. The latter two

Пункт 2: гидростатическое равновесие газового слоя

2.2 Vertical Force Balance

A second ansatz of our model, following a number of authors (e.g., Boulares & Cox 1990; Piontek & Ostriker 2007; Koyama & Ostriker 2009; Ostriker, McKee & Leroy 2010) is that the gas is in vertical hydrostatic equilibrium. The spatially-averaged momentum equation for a time-steady isothermal gas reads (Krumholz 2017, equation 10.9; also see Kim & Ostriker 2015b)

$$\frac{\partial}{\partial z}\left\langle \rho_{\rm g}\left(\sigma_{\rm th}^2+v_z^2+v_A^2\right)\right\rangle-\frac{\partial}{\partial z}\left\langle\frac{B_z^2}{4\pi}\right\rangle-\langle\rho_{\rm g}g_z\rangle=0 \quad (10)$$

where $\rho_{\rm g}$ is the gas density, $\sigma_{\rm th}$ is the gas thermal velocity dispersion, v_z is the vertical velocity, v_A is the gas Alfvén speed, B_z is the z component of the magnetic field, g_z is the vertical gravitational acceleration, and we have oriented our coordinate system so the disc midplane lies in the xy plane; the angle brackets denote averaging over the area of the disc, where the area considered is small compared to the disc scale length, but large compared to the size of an individual molecular cloud of star-forming complex. The first

$$\frac{1}{r}\frac{\partial}{\partial r}\left(r\frac{\partial\psi}{\partial r}\right)+\frac{\partial^2\psi}{\partial z^2}=4\pi G\rho, \quad (13)$$

where ρ is the total density including all components. The radial gradient of ψ is related to the rotation curve by

$$\frac{v_\phi^2}{r}=\frac{\partial\psi}{\partial r}, \quad (14)$$

and using this in the Poisson equation we obtain

$$\frac{\partial g_z}{\partial z}=4\pi G\rho-2\beta\Omega^2, \quad (15)$$

where $g_z=\partial\psi/\partial z$. Integrating, we therefore have

$$g_z\approx\int_0^z\left(4\pi G\rho-2\beta\Omega^2\right)\,dz'. \quad (16)$$

Note that, although it is tempting to approximate that $\beta\Omega^2$ is constant for small z, this approximation clearly fails for the common case of a flat rotation curve, $\beta=0$, because $\beta=0$ at the midplane but not above it – see Appendix C of McKee, Parravano & Hollenbach (2015) for discussion. The weight is therefore

$$\int_0^\infty\langle\rho_{\rm g}g_z\rangle\,dz=2\pi G\int_0^\infty\rho_{\rm g}\left[\Sigma(z)-\frac{1}{\pi G}\int_0^z\beta\Omega^2\,dz'\right]dz \quad (17)$$

Пункт 3: баланс энергии, с фидбэком от звезд и радиальным переносом газа

Our model is based on the realisation that there is an alternative source of energy, radial transport. Such transport injects energy at scales comparable to the gas scale height, which then cascades down to become turbulent on smaller scales. Krumholz & Burkert (2010) show that the time evolution of the gas velocity dispersion obeys

$$\frac{\partial \sigma_{\rm g}}{\partial t} = \frac{\mathcal{G}-\mathcal{L}}{3\sigma_{\rm g}\Sigma_{\rm g}} + \frac{\sigma_{\rm g}}{6\pi r\Sigma_{\rm g}}\frac{\partial \dot{M}}{\partial r} + \frac{5(\partial\sigma_{\rm g}/\partial r)}{6\pi r\Sigma}\dot{M} - \frac{1-\beta}{6\pi r^2\Sigma_{\rm g}\sigma_{\rm g}}\Omega\mathcal{T}, \quad (36)$$

where $\mathcal{T}$ is the torque exerted by non-axisymmetric stresses, and

$$\dot{M} = -\frac{1}{v_\phi(1+\beta)}\frac{\partial \mathcal{T}}{\partial r} \quad (37)$$

is the rate of inward mass accretion through the disc. There is clear physical interpretation for equation 36. The first term on the right hand side is the net effect of star formation driving ($\mathcal{G}$) and dissipation of turbulence ($\mathcal{L}$), the second and third represent advection of kinetic energy as gas moves through the disc, and the final term represents transfer of energy from the galactic gravitational potential to the gas.

If we search for solutions where that gas is in energy equilibrium, $\partial\sigma_{\rm g}/\partial t = 0$, then equation 36 implies that

$$\frac{\sigma_{\rm g}^2}{2\pi r}\frac{\partial \dot{M}}{\partial r} + \frac{5\sigma_{\rm g}\dot{M}}{2\pi r}\frac{\partial \sigma_{\rm g}}{\partial r} - \frac{1-\beta}{2\pi r^2}\Omega\mathcal{T} = \mathcal{L}-\mathcal{G} \quad (38)$$

Примеры моделей для разных типов галактик

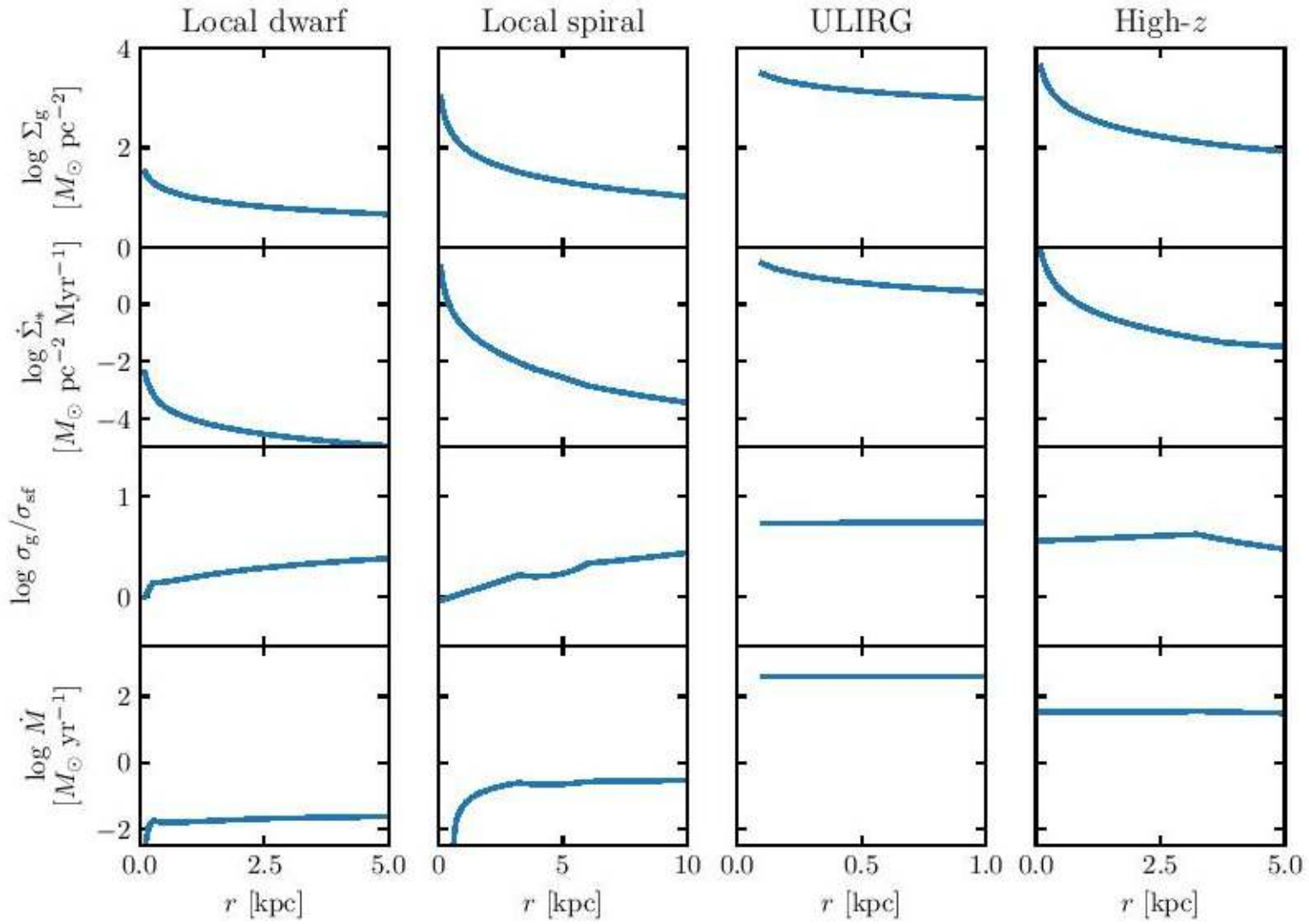

Закон Кенниката-Шмидта воспроизводится

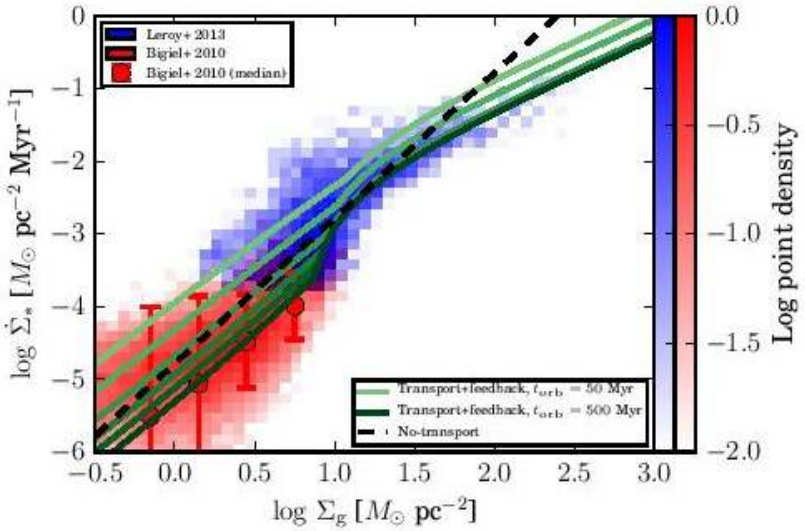

Figure 2. Comparison between theoretical models predictions of the star formation law and observation of nearby galaxies at $\sim$ 1 kpc resolution. Lines represent models; solid green lines are the transport+feedback model (equation 32), evaluated for orbital times evenly spaced in logarithm from $t_{\rm orb} = 50 - 500$ Myr, with lighter colours (toward the top) corresponding to shorter orbital times. The dashed black line is the no-transport model (equation 56), which has no dependence on orbital time. All models use the fiducial parameters given in Table 1, and we compute the star-forming molecular fraction $f_{\rm sf}$ from the KMT+ model (Krumholz 2013) as in Section 2.4.3, using a Solar-normalised metallicity $Z' = 1/3$, appropriate for dwarfs and outer discs. Coloured histograms show observations; colours indicate the distribution of individual pixels in the $\Sigma_{\rm g} - \dot{\Sigma}_*$ plane for inner galaxies (blue; Leroy et al. 2013) and outer galaxies and dwarfs (red; Bigiel

… только если есть и фидбэк, и перенос

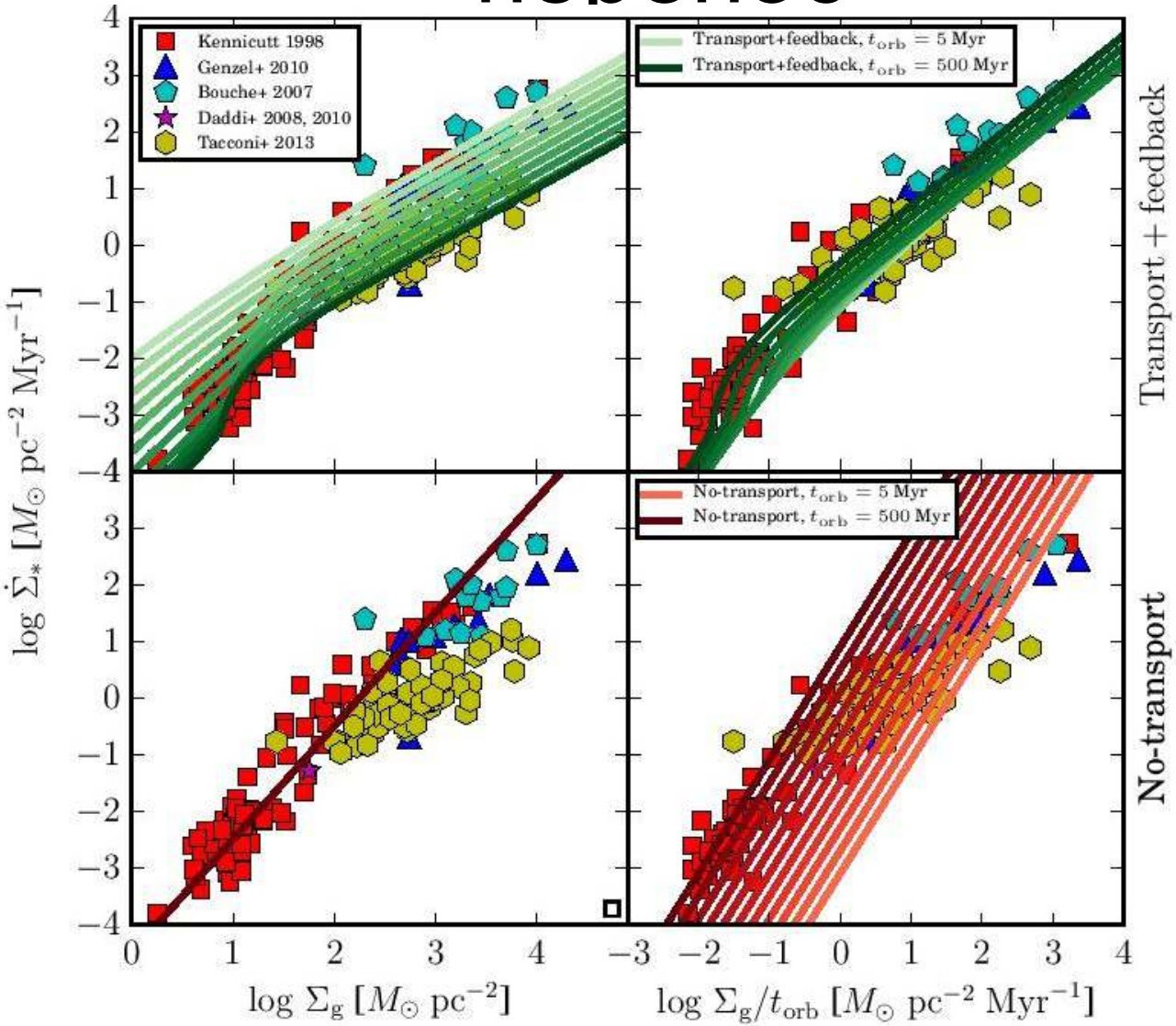

Про дисперсию скоростей газа

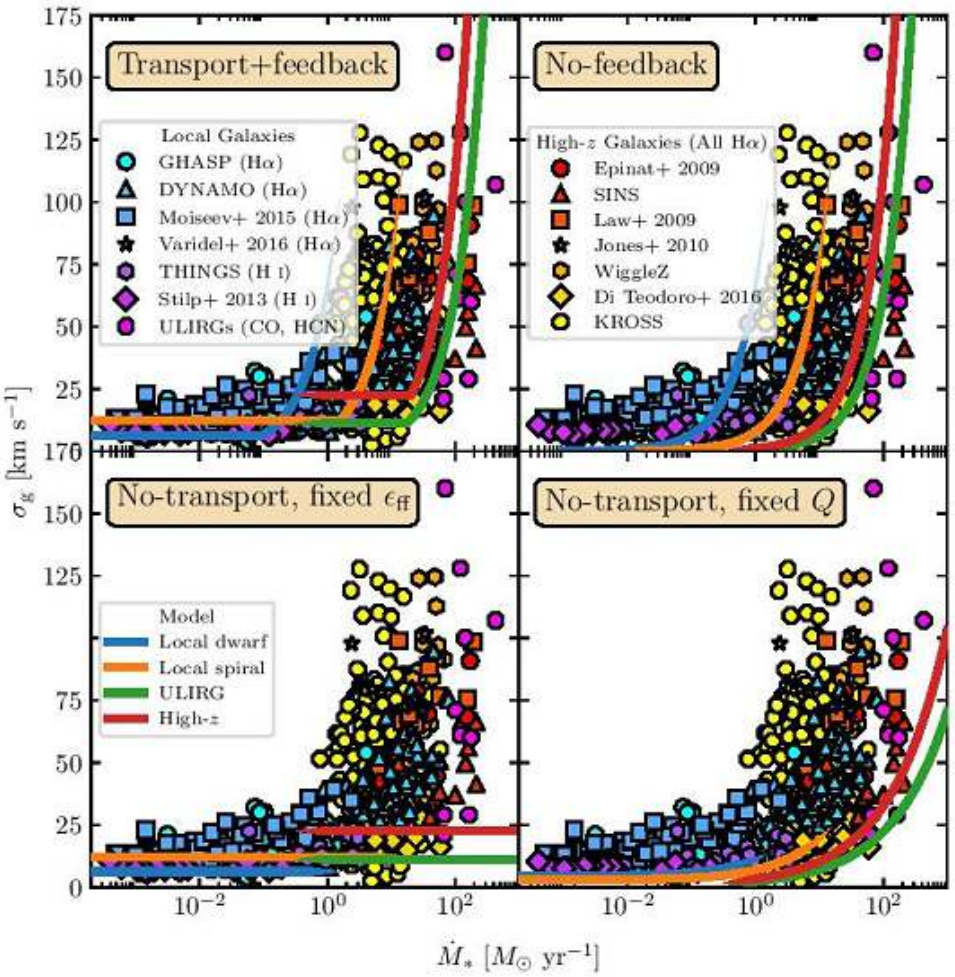

Спекуляции про эволюцию – все зависит от темпа аккреции

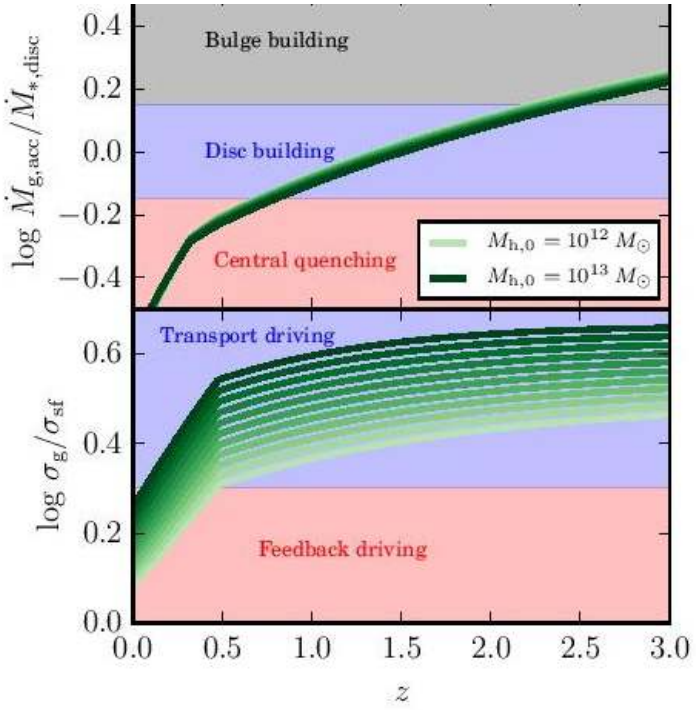

Figure 7. Evolution of the ratio of gas accretion rate to disc star formation rate (top panel) and gas velocity dispersion to star formation-supported velocity dispersion (bottom panel) as a function of redshift. Each line represents the evolutionary path of a particular halo, with the lightest colour (bottom lines in the lower panel) corresponding to a halo with a present-day mass of $M_{h,0} = 10^{12}\ M_\odot$, and the darkest (top lines in the lower panel) to a halo with a present-day mass of $M_{\rm h,0} = 10^{13}\ M_\odot$. Intermediate lines

Astro-ph: 1705.10283

CO-dark molecular gas at high redshift: very large H_2 content and high pressure in a low metallicity damped Lyman-alpha system

S.A. Balashev [1]*, P. Noterdaeme [2], H. Rahmani [3,4], V.V. Klimenko [1], C. Ledoux [5], P. Petitjean [2], R. Srianand [6], A.V. Ivanchik [1], D.A. Varshalovich [1]

[1] *Ioffe Institute of RAS, Polytekhnicheskaya 26, 194021 Saint-Petersburg, Russia*
[2] *Institut d'Astrophysique de Paris, CNRS-UPMC, UMR7095, 98bis bd Arago, 75014 Paris, France*
[3] *Aix Marseille Université, CNRS, LAM (Laboratoire d'Astrophysique de Marseille) UMR 7326, 13388, Marseille, France*
[4] *School of Astronomy, Institute for Research in Fundamental Sciences (IPM), P.O. Box 19395-5531, Tehran, Iran*
[5] *European Southern Observatory, Alonso de Córdova 3107, Vitacura, Casilla 19001, Santiago 19, Chile*
[6] *Inter-University Centre for Astronomy and Astrophysics, Post Bag 4, Ganeshkhind, 411 007 Pune, India*

Accepted 2017 May 26; in original form 2017 February 17

ABSTRACT

We present a detailed analysis of a H_2-rich, extremely strong intervening Damped Ly-α Absorption system (DLA) at $z_{abs} = 2.786$ towards the quasar J0843+0221, observed with the Ultraviolet and Visual Echelle Spectrograph on the Very Large Telescope. The total column density of molecular (resp. atomic) hydrogen is $\log N(H_2)=21.21 \pm 0.02$ (resp. $\log N(\mathrm{H\,I})=21.82 \pm 0.11$), making it to be the first case in quasar absorption lines studies with H_2 column density as high as what is seen in ^{13}CO-selected clouds in the Milky-Way.

Линия Лайман-альфа

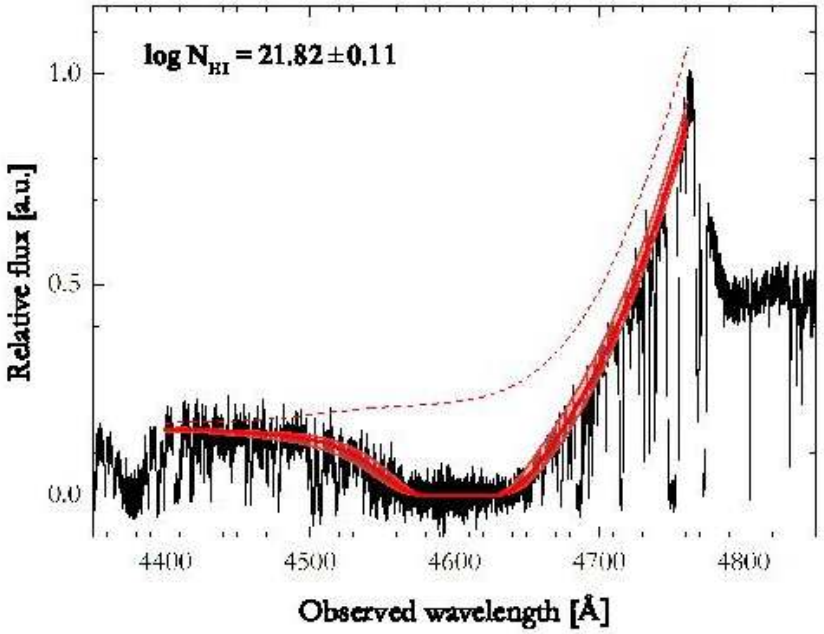

Figure 1. A portion of our UVES spectrum around the DLA at $z = 2.786$. The solid red line represents the fitted Ly-α profile with associated uncertainty as shaded region. The red dashed line shows the reconstructed continuum, which was fitted together with the H I line profile. The measured H I column density is $\log N(\mathrm{H\,I}) = 21.82 \pm 0.11$, i.e. this DLA corresponds to a sub-class of DLA known as extremely strong DLAs (ESDLAs, Noterdaeme et al. 2014).

Колебательные линии H_2

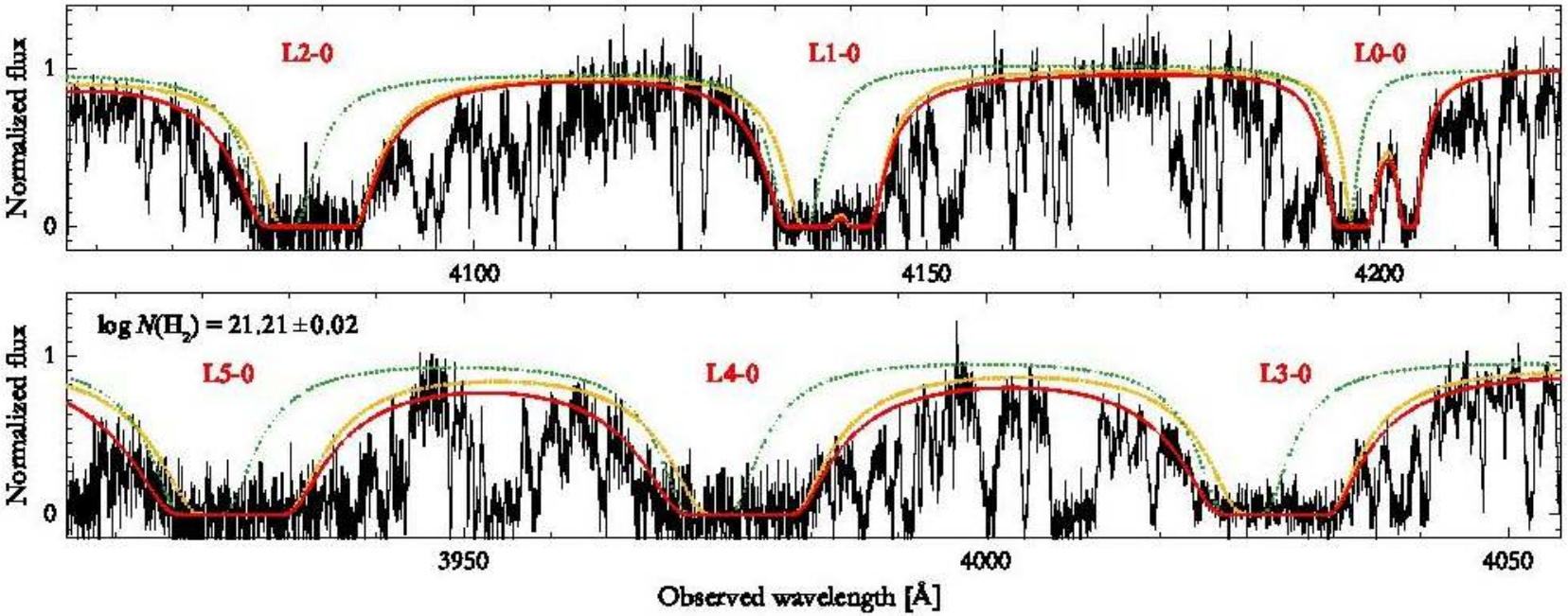

Figure 3. Portion of our UVES spectrum of J0843+0221 around the region of H_2 absorption lines from the DLA at $z = 2.786$. The red solid line shows the total fitted profile to the $J = 0$ and $J = 1$ absorption lines, while green and orange dashed lines represent the contribution of the $J = 0$ and $J = 1$ levels, respectively. This is the largest H_2 column density DLA detected in QSO spectra.

Другие линии

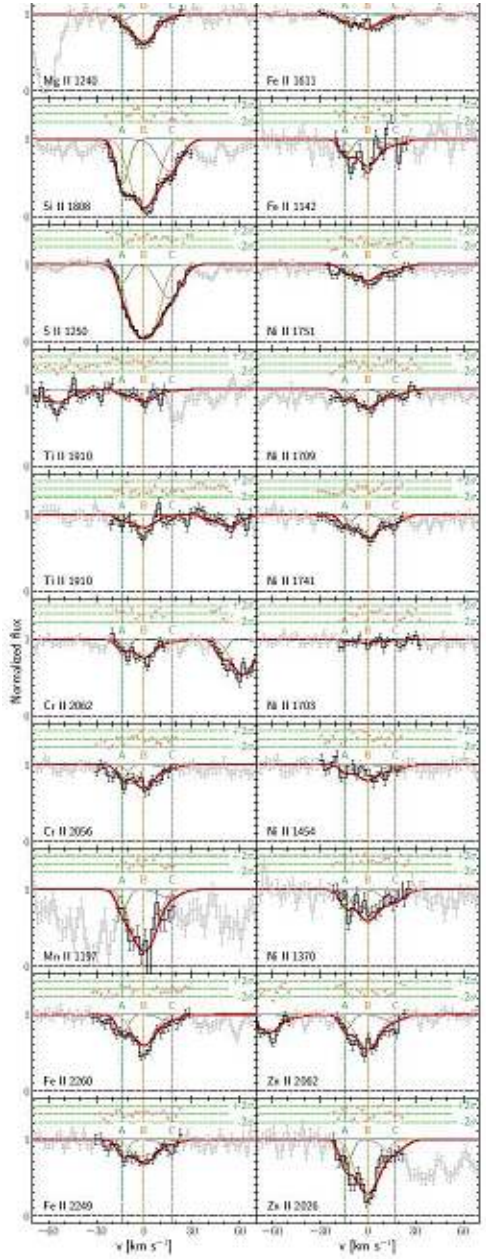

4.1 Metallicity and depletion pattern

For each element we determine the abundance relative to Solar values from Asplund et al. (2009), without applying any ionization correction (i.e. we assume all metals to be in their main ionization state). This is a fairly reasonable assumption given the large H I column density in this DLA. Since we cannot determine the hydrogen column density in individual components, we derive gas phase abundances using the total hydrogen column density $N(\mathrm{H}) = 21.99^{+0.08}_{-0.07}$ and the total metal column densities, see Table 2.

The observed gas-phase abundances of zinc and sulphur are usually considered as good indicators of the ISM metallicity since these are non-refractory elements for which dust depletion corrections are expected to be negligible. Their abundances, $[\mathrm{Zn/H}] = -1.52^{+0.08}_{-0.10}$ and $[\mathrm{S/H}] = -1.54^{+0.08}_{-0.08}$ are indeed in very good agreement.

Table 2. Summary of the overall gas-phase abundances

Species (X)	[X/H]
Cl I	$-1.86^{+0.21}_{-0.10}$
Mg II	$-1.65^{+0.09}_{-0.10}$
Si II	$-1.73^{+0.08}_{-0.10}$
S II	$-1.54^{+0.08}_{-0.08}$
Ti II	$-1.96^{+0.10}_{-0.11}$
Cr II	$-2.40^{+0.09}_{-0.10}$
Mn II	$-1.75^{+0.10}_{-0.10}$
Fe II	$-2.53^{+0.08}_{-0.10}$
Ni II	$-2.52^{+0.09}_{-0.10}$
Zn II	$-1.52^{+0.08}_{-0.10}$

Температура повышенная

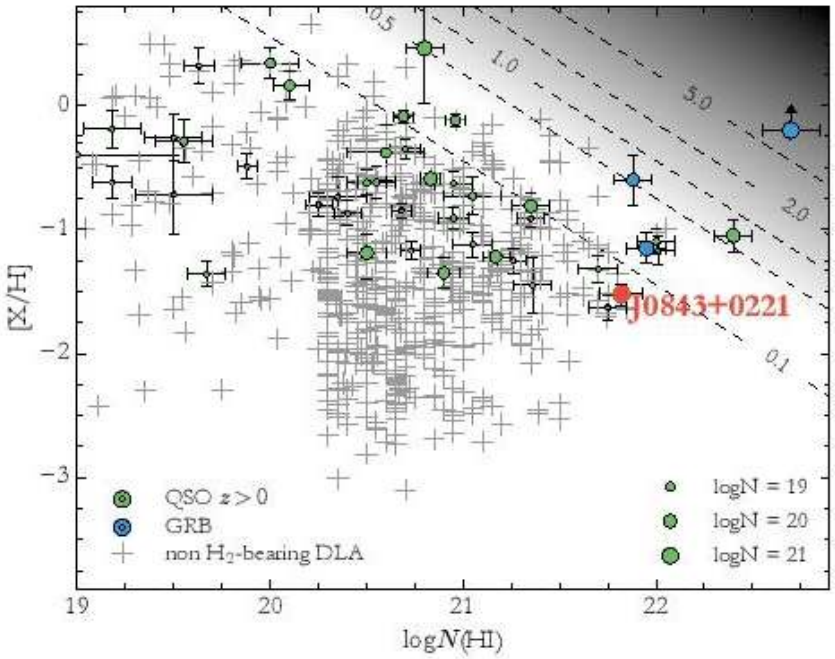

Figure 11. Metallicity versus H I column density in DLAs. The green and blue circles indicate the H_2-bearing DLAs at high redshifts detected towards QSO and in GRB afterglows, respectively. The size of each circle depends on H_2 column density. The grey crosses correspond to non H_2-bearing DLAs. The dashed black lines show constant value of A_V calculated in the assumption to fixed scale factor between metallicity and dust abundance corresponds to the Milky-Way measurements. The shaded region reflects systematic bias due to obscuration.

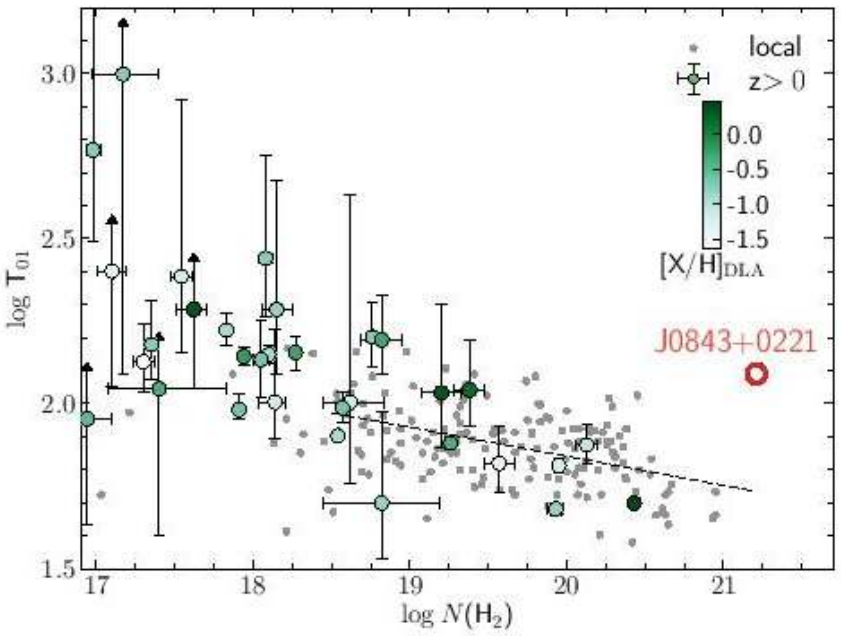

Figure 12. Measurements of the H_2 excitation temperature, T_{01} at different $N(H_2)$. The grey points represent measurements in the local group (MW, SMC and LMC). Filled circles represent measurements at $z > 0$, where the color corresponds to the average metallicity of each associated DLA. The measurement in the DLA towards J 0843+0221 is at least a factor of two higher than the value expected from extrapolating the trend of decreasing T_{01} with increasing $N(H_2)$.

… а давление нормальное

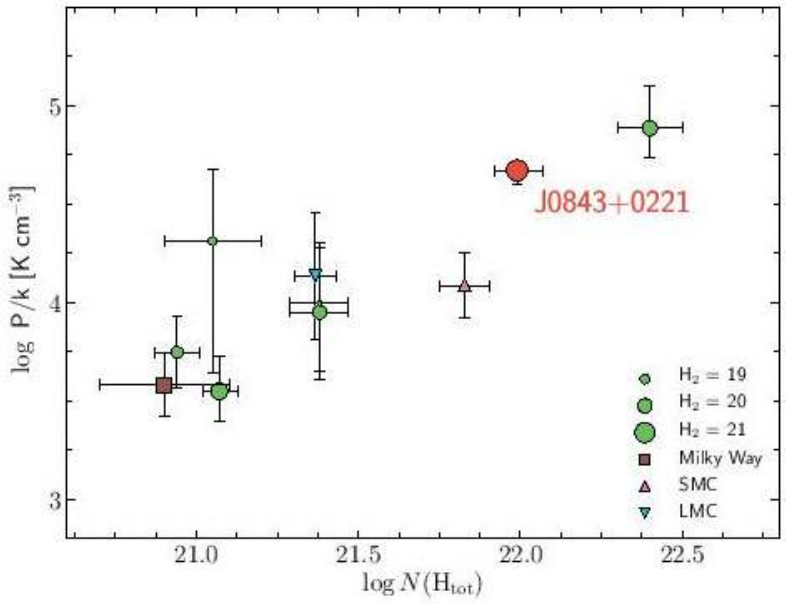

Figure 14. Estimated thermal pressure versus total hydrogen column density. Circles represent values derived from the C I fine structure levels together with the H_2 excitation temperature, T_{01}. The size of each circle corresponds to the H_2 column density. Squares correspond to the *average* values found in the local group (Milky Way, SMC and LMC). Measurement in the DLA towards J 0843+0221 is consistent with increase of the thermal pressures with increasing log N(H).

CO-dark газ

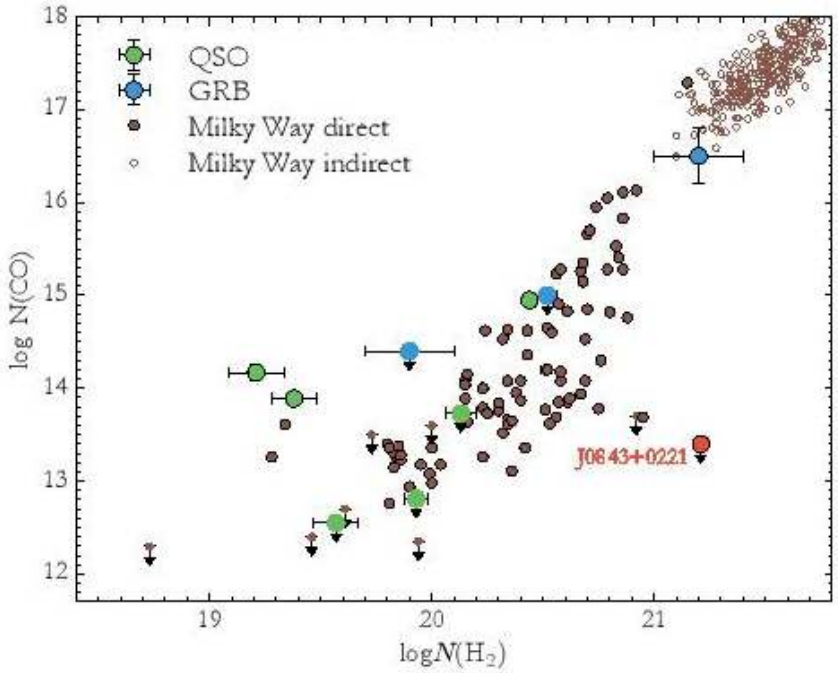

Figure 17. Dependence of N(CO) to $N(H_2)$ column densities for high redshift DLAs detected in quasar and GRB afterglow (green and blue points, respectively). The open and filled brown points correspond to direct (Shefer et al. 2008; Burgh et al. 2009) and indirect (Federman et al. 1990) H_2 measurements in our Galaxy, respectively. The upper limit on N(CO) in the H_2 absorption system at z=2.7865 studied here is shown by a red circle

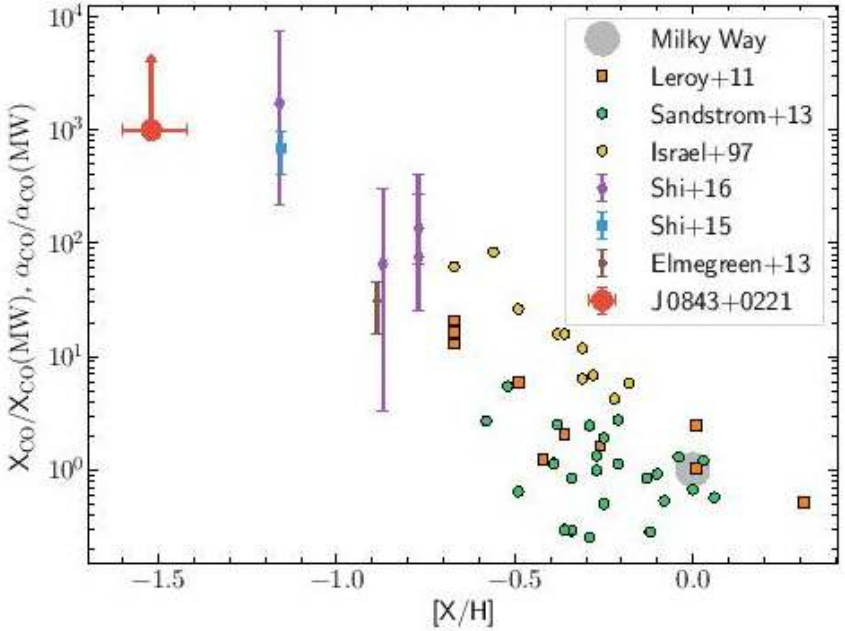

Figure 18. Measurements of X_{CO} and α_{CO} conversion factors relative to adopted Milky Way values (Bolatto et al. 2013) as a function of metallicity. The data for the local measurements of α_{CO} are from Israel & P. 1997; Leroy et al. 2011; Sandstrom et al. 2013; Elmegreen et al. 2013; Shi et al. 2015, 2016.

Astro-ph: 1705.10521

A star formation study of the ATLAS^{3D} early-type galaxies with the AKARI all-sky survey

T. Kokusho[1], H. Kaneda[1], M. Bureau[2], T. Suzuki[1], K. Murata[1], A. Kondo[1], and M. Yamagishi[3]

[1] Graduate School of Science, Nagoya University, Chikusa-ku, Nagoya 464-8602, Japan
e-mail: kokusho@u.phys.nagoya-u.ac.jp
[2] Sub-department of Astrophysics, Department of Physics, University of Oxford, Denys Wilkinson Building, Keble Road, Oxford OX1 3RH, UK

[3] Institute of Space and Astronautical Science, Japan Aerospace Exploration Agency, Chuo-ku, Sagamihara 252-5210, Japan

May 31, 2017

Что такое AKARI

The new IR fluxes presented here were obtained from the AKARI satellite (Murakami et al. 2007) all-sky surveys in the MIR (central wavelengths 9 and 18 μm; Onaka et al. 2007) and FIR (65, 90 and 140 μm; Kawada et al. 2007). For the MIR 9 and 18 μm bands, the total galaxy flux densities were obtained through aperture photometry as follows. First, we applied a spatial filtering of 1.3 arcmin^{-1} to each galaxy image, to remove periodic noise. Second, we performed aperture photometry on the all-sky diffuse maps (Doi et al. 2015; Ishihara et al., in preparation), within a circular aperture of radius $R_{\rm aper} = \sqrt{(2R_{\rm e})^2 + (1.5D_{\rm PSF})^2}$, where $R_{\rm e}$ is the effective radius of each galaxy in the optical B band (Cappellari et al. 2011) and $D_{\rm PSF}$ is the full width at half maximum of the point spread function (PSF) of the AKARI instrument at the given wavelength (Ishihara et al. 2010; Takita et al. 2015). The average sky level was first measured in a circular annulus of inner radius $1.5R_{\rm aper}$ and outer radius $2.5R_{\rm aper}$, and was then subtracted from individ-

Только там, где есть CO, - избыток инфракрасного излучения

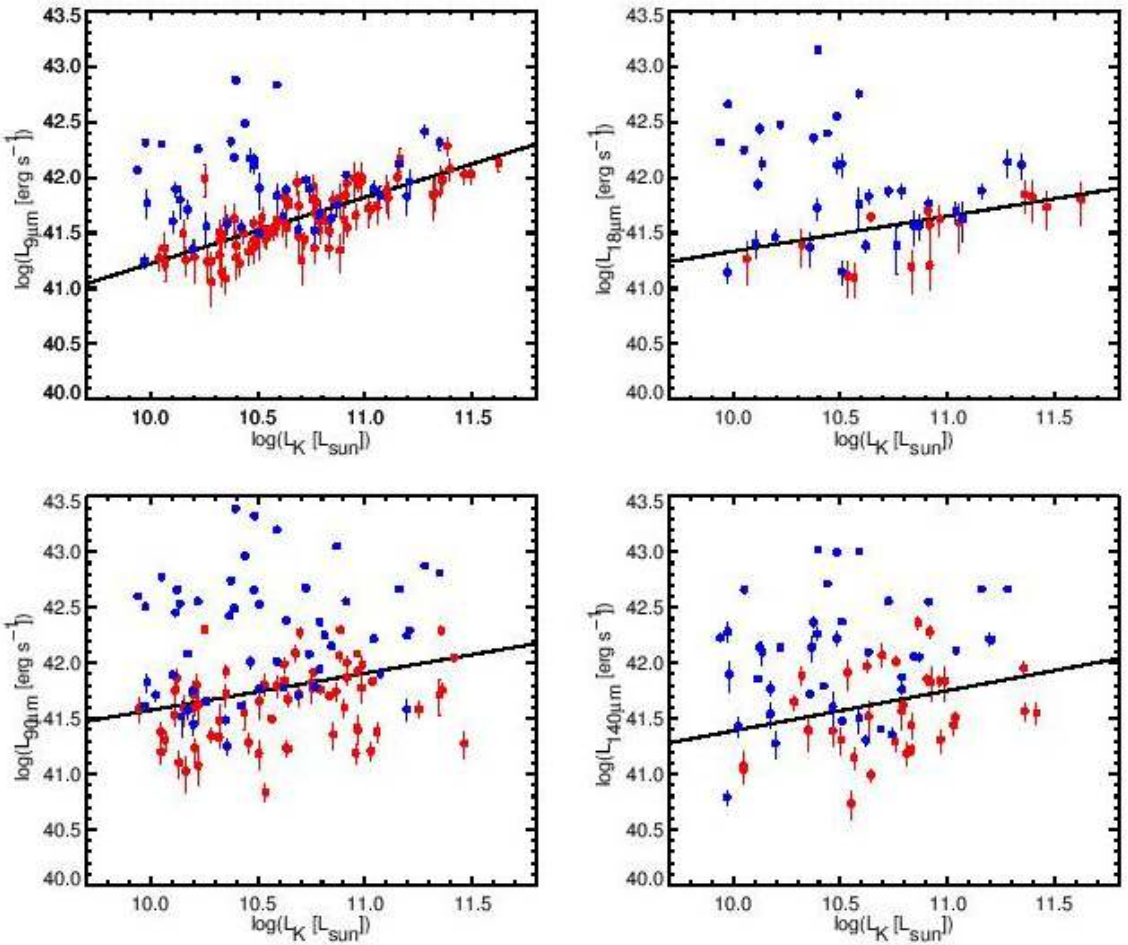

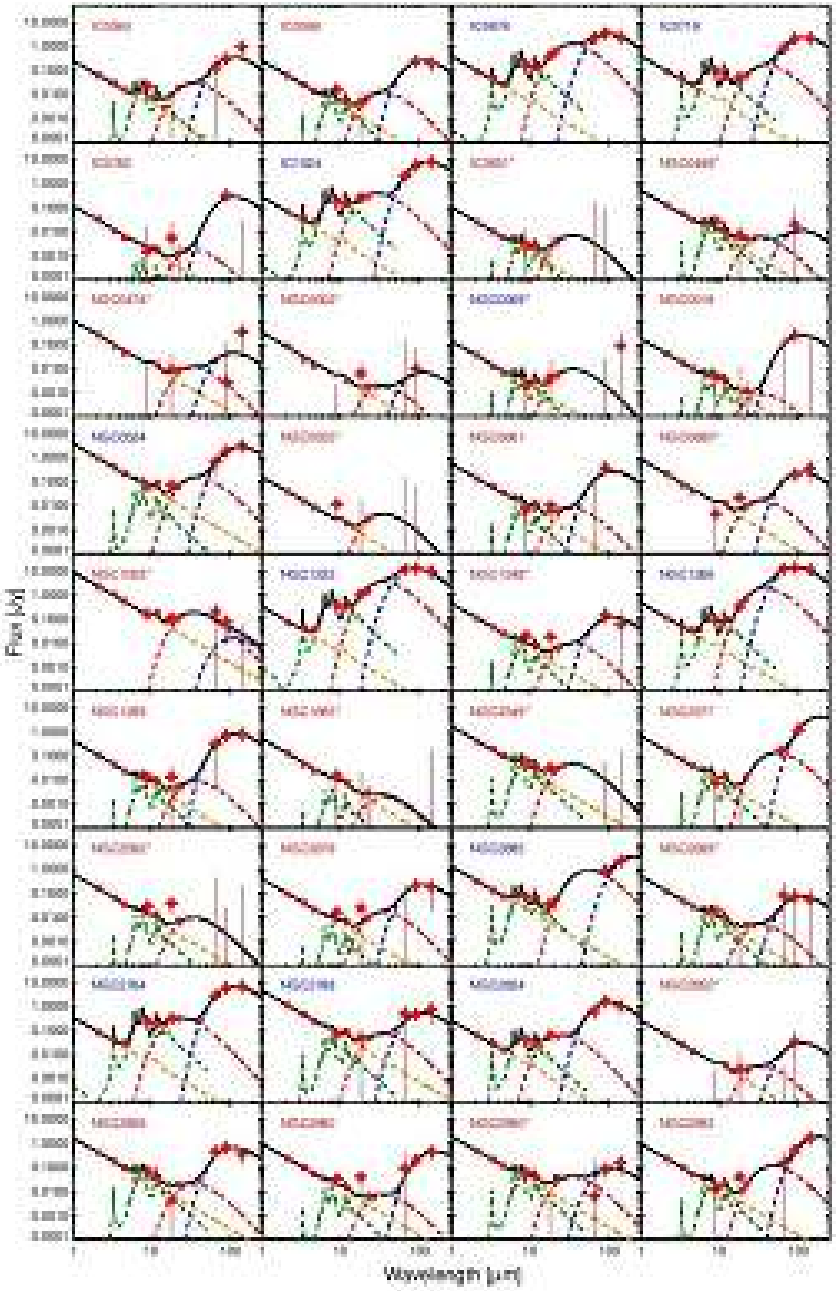

Пример SEDов

Кенникат-Шмидт для галактик ранних типов

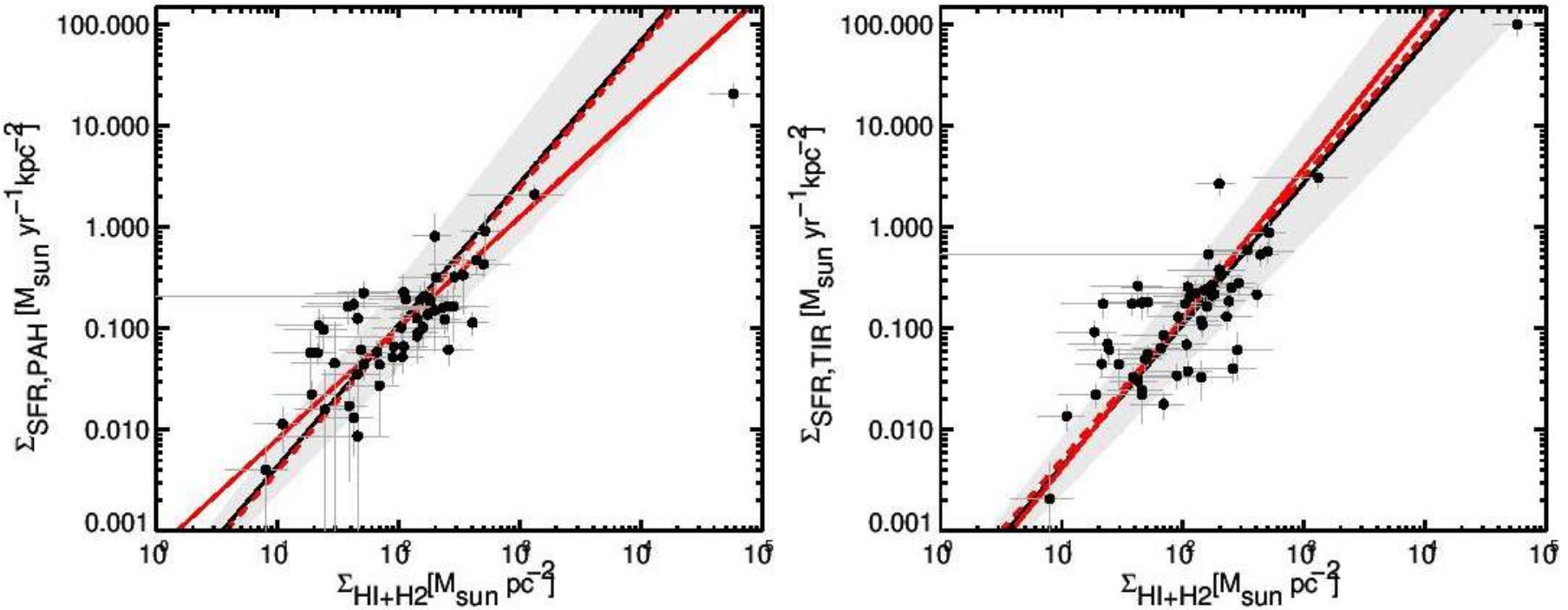

Fig. 7. Star formation rates (PAH- and TIR-derived) versus total gas surface densities (i.e., KS law) for CO-detected galaxies. Solid black lines and shaded grey regions show respectively the Kennicutt (1998) relation for local star-forming galaxies (with power-law index $n = 1.4$) and its intrinsic scatter. Solid and dashed red lines show the best linear fits with respectively free and fixed ($n = 1.4$) slope. The galaxy located in the top-right of each panel is NGC 1266, known to have strongly suppressed star formation. It was excluded from the fits.

Эффективность звездообразования - постоянна

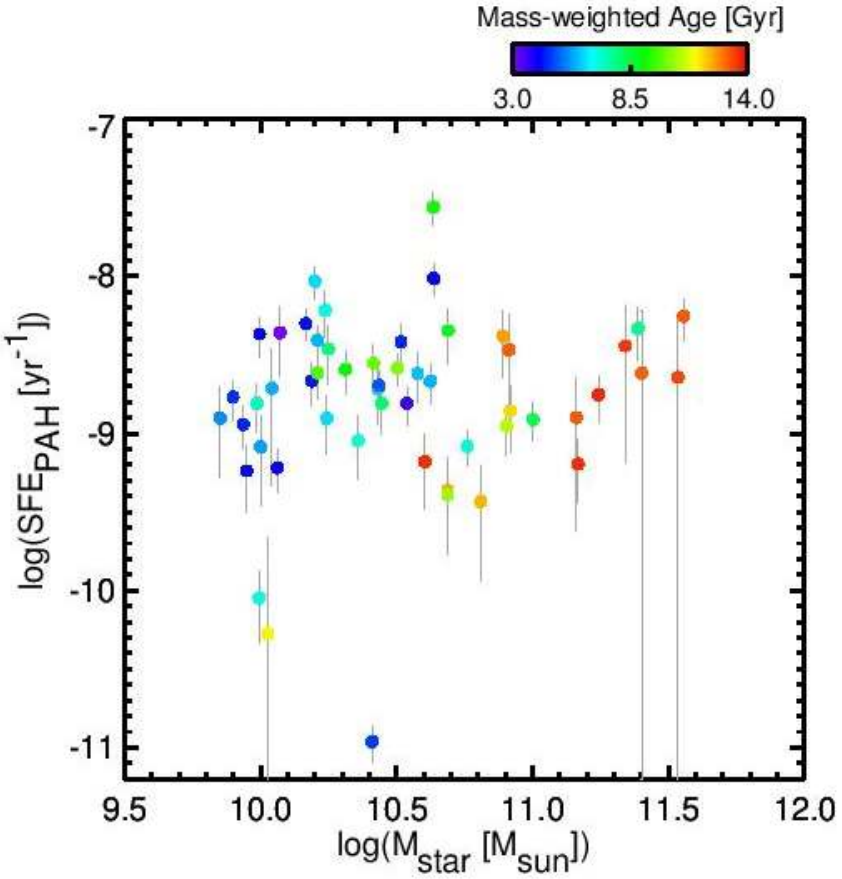

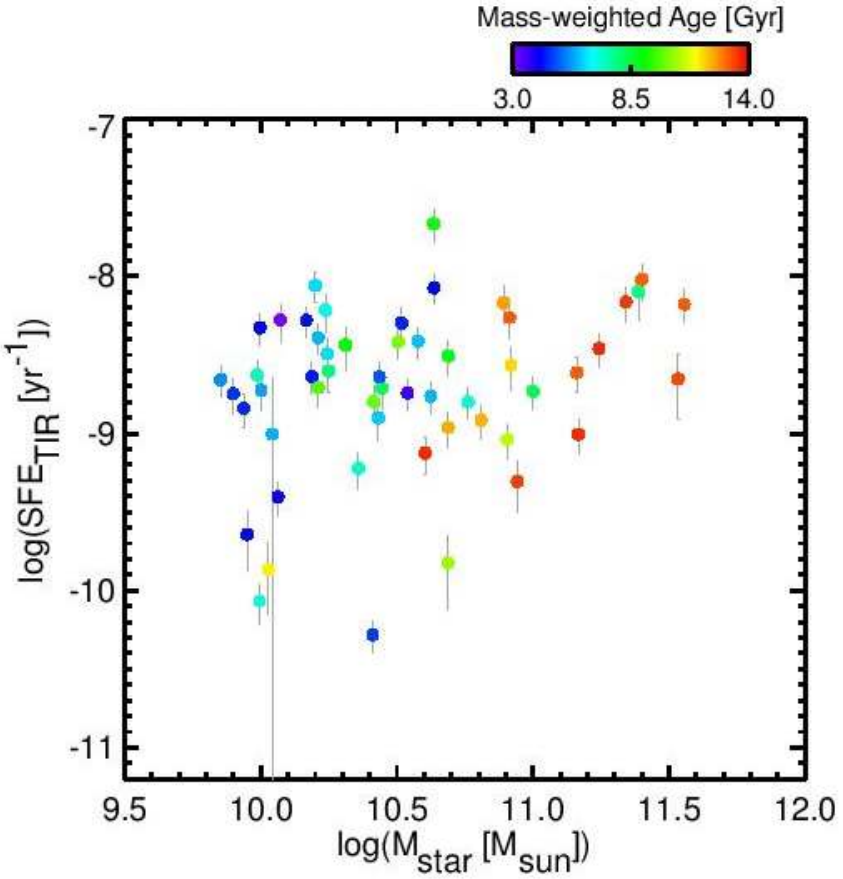

Astro-ph: 1705.10849

GALAXY MERGER CANDIDATES IN HIGH-REDSHIFT CLUSTER ENVIRONMENTS

A. G. Delahaye [1], T. M. A. Webb[1], J. Nantais[2] A. DeGroot[3], G. Wilson[3], A. Muzzin[4], H. K. C. Yee[5], R. Foltz[3], A. G. Noble[6], R. Demarco[7], A. Tudorica[8], M. C. Cooper[9], C. Lidman[10], S. Perlmutter[11,12], B. Hayden[11,12], K. Boone[11,12], J. Surace[13]

Draft version June 1, 2017

ABSTRACT

We compile a sample of spectroscopically- and photometrically-selected cluster galaxies from four high-redshift galaxy clusters ($1.59 < z < 1.71$) from the *Spitzer* Adaptation of the Red-Sequence Cluster Survey (SpARCS), and a comparison field sample selected from the UKIDSS Deep Survey. Using near-infrared imaging from the *Hubble Space Telescope* we classify potential mergers involving massive ($M_* \geq 3 \times 10^{10} \mathrm{M}_\odot$) cluster members by eye, based on morphological properties such as tidal distortions, double nuclei, and projected near neighbors within 20 kpc. With a catalogue of 23 spectroscopic and 32 photometric massive cluster members across the four clusters and 65 spectroscopic and 26 photometric comparable field galaxies, we find that after taking into account contamination from interlopers, $11.0^{+7.0}_{-5.6}\%$ of the cluster members are involved in potential mergers, compared to $24.7^{+5.3}_{-4.6}\%$ of the field galaxies. We see no evidence of merger enhancement in the central cluster environment with respect to the field, suggesting that galaxy-galaxy merging is not a stronger source of galaxy evolution in cluster environments compared to the field at these redshifts.

Выборка скоплений

TABLE 1
CLUSTER PROPERTIES

Cluster ID	RA	Dec	z	Spec Members	*HST* Imaging	Exposure Times
SpARCS-J0225[a]	02 : 25 : 45.6	−03 : 55 : 17.1	1.598	8	F160W	2424s
SpARCS-J0330[b]	03 : 30 : 55.9	−28 : 42 : 59.5	1.626	38	F105W, F140W, F160W	10775s, 11625s, 5019s
SpARCS-J0224[b,c]	02 : 24 : 26.3	−03 : 23 : 30.8	1.633	45	F105W, F140W, F160W	7581s, 9829s, 6116s
SpARCS-J1049[d]	10 : 49 : 22.6	+56 : 40 : 32.6	1.709	27	F105W, F160W	8543s, 9237s

[a] Nantais et al. (2016)
[b] Lidman et al. (2012)
[c] Muzzin et al. (2013)
[d] Webb et al. (2015a)

Пример классификации

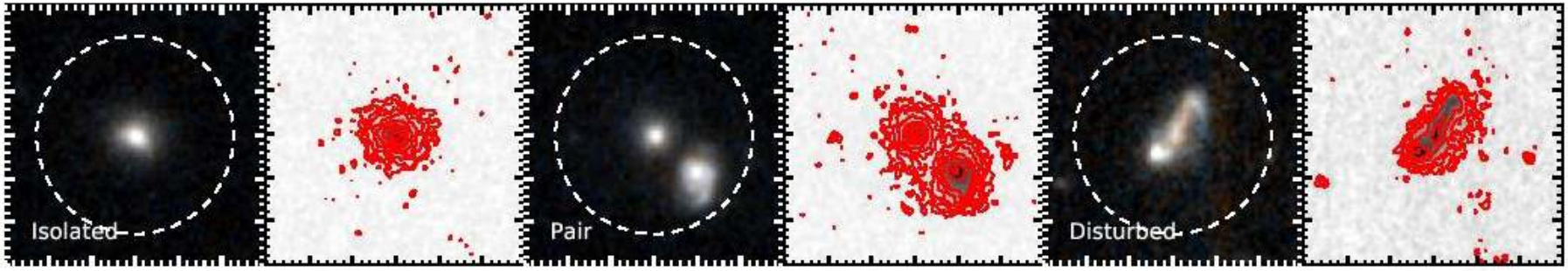

FIG. 1.— Examples of galaxies identified in each of the three classifications from the UDS control sample. Left panels are RGB images with filters F160W, F125W+F160W, F125W with a 20 kpc radius circle overlaid, and right panels are F160W grayscale maps with surface brightness shown as 0.5 mag arcsec^{-2} contours. The galaxy in the left stamp is identified as isolated, with no near neighbor within the 20 kpc radius and no significant asymmetry or distortion. The galaxy in the central stamp has a clear near neighbor within 20 kpc. The galaxy in the right stamp shows signs of tidal distortion and strong asymmetry with no clear counterpart.

Результат: в скоплениях галактики сливаются реже, чем в поле

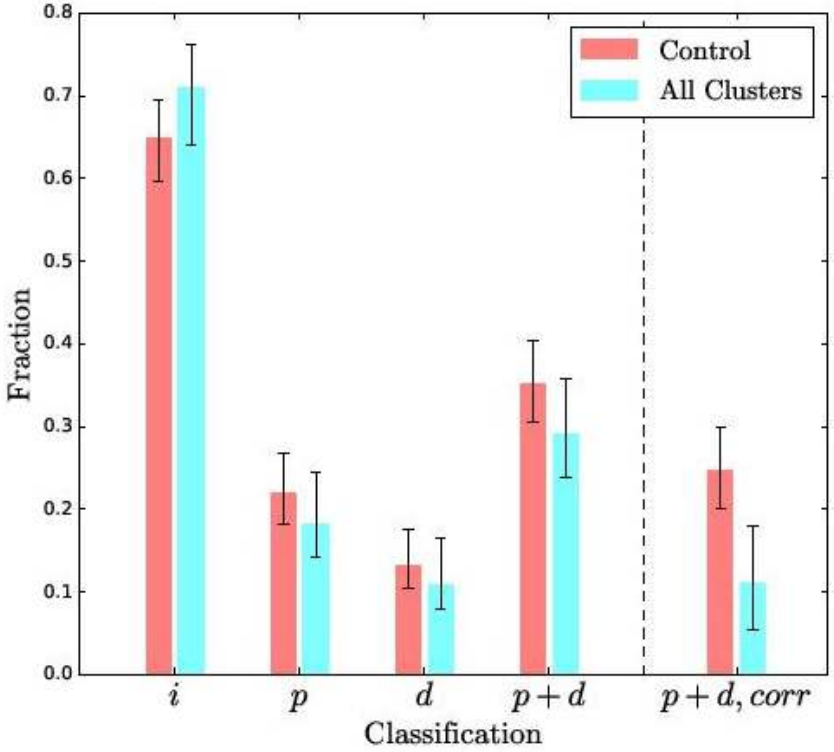

FIG. 4.— Fraction of galaxies found under each classification for UDS control sample and combined cluster sample. Left to right are isolated, pairs, disturbed, combined pairs + disturbed (representing overall merger probability) and combined pairs + disturbed after being corrected for interlopers. Errorbars show 68% confidence and were estimated assuming a binomial distribution and utilizing the beta function.